Soft and anisotropic local moments in 4d and 5d mixed-valence M2O9 dimers

Ying Li, Alexander A. Tsirlin, Tusharkanti Dey, Philipp Gegenwart, Roser Valentí, Stephen M. Winter

Angaben zur Veröffentlichung / Publication details:

Li, Ying, Alexander A. Tsirlin, Tusharkanti Dey, Philipp Gegenwart, Roser Valentí, and Stephen M. Winter. 2020. "Soft and anisotropic local moments in 4d and 5d mixed-valence M2O9 dimers." *Physical Review B* 102 (23): 235142. https://doi.org/10.1103/physrevb.102.235142.

Soft and anisotropic local moments in 4*d* and 5*d* mixed-valence M_2O_9 dimers

Ying Li [1,2,*] Alexander A. Tsirlin [3] Tusharkanti Dey [3,†] Philipp Gegenwart [3]
Roser Valentí [2,‡] and Stephen M. Winter [2,§]

[1]*Department of Applied Physics and MOE Key Laboratory for Nonequilibrium Synthesis and Modulation of Condensed Matter, School of Physics, Xi'an Jiaotong University, Xi'an 710049, China*

[2]*Institut für Theoretische Physik, Goethe-Universität Frankfurt, Max-von-Laue-Strasse 1, 60438 Frankfurt am Main, Germany*

[3]*Experimental Physics VI, Center for Electronic Correlations and Magnetism, University of Augsburg, 86159 Augsburg, Germany*

(Received 28 April 2020; revised 25 November 2020; accepted 30 November 2020; published 18 December 2020)

We investigate via exact diagonalization of finite clusters the electronic structure and magnetism of M_2O_9 dimers in the mixed-valence hexagonal perovskites $A_3B'M_2O_9$ for various different fillings of 4*d* and 5*d* transition-metal M ions. We find that the magnetic moments of such dimers are determined by a subtle interplay of spin-orbit coupling, Hund's coupling, and Coulomb repulsion, as well as the electron filling of the M ions. Most importantly, the magnetic moments are anisotropic and temperature dependent. This behavior is a result of spin-orbit coupling, magnetic field effects, and the existence of several nearly degenerate electronic configurations whose proximity allows the occupation of excited states already at room temperature. This analysis is consistent with experimental susceptibility measurements for a variety of dimer-based materials. Furthermore, we perform a survey of $A_3B'M_2O_9$ materials and propose ground-state phase diagrams for the experimentally relevant M fillings of $d^{4.5}$, $d^{3.5}$, and $d^{2.5}$. Finally, our results show that the usually applied Curie-Weiss law with a constant magnetic moment cannot be used in these spin-orbit-coupled materials.

DOI: 10.1103/PhysRevB.102.235142

I. INTRODUCTION

Oxides of 4*d* and 5*d* transition metals feature strong spin-orbit coupling, moderate electronic correlations, and sizable metal-oxygen hybridization. Together, these effects may give rise to exotic spin-orbital states, including quantum spin liquids relying on strongly anisotropic effective magnetic Hamiltonians [1–5]. An interesting class of such materials is the 6H perovskite family $A_3B'M_2O_9$ (M = Ir, Os, Re, Rh, Ru), which features face-sharing M_2O_9 dimers as the central magnetic and structural unit. Whereas the A-cations are almost always divalent, the oxidation state of the B′-cations ranges from 1+ to 4+, thus imposing different charge states to the transition metal M. Compounds with integer oxidation states of M usually behave as common spin dimers [6,7], where two magnetic centers are coupled by a moderately strong exchange interaction leading to a nonmagnetic ground state. However, in $5d^4$ systems with the nonmagnetic ($J_{\rm eff} = 0$) state of individual M ions, unusual effects like "excitonic" magnetism can be expected [8] if interdimer magnetic couplings exceed the energy gap to excited multiplets with $J_{\rm eff} > 0$. The $Ba_3B'Ir_2O_9$ iridates with divalent B′ = Zn, Ca, Sr serve as possible experimental examples for this scenario [9,10].

In contrast, if the total charge of $[A_3B']$ is odd, it induces a half-integer oxidation state in M, i.e., a mixed (or intermediate) valence of the transition-metal ion [11]. In this case, having an odd number of electrons per dimer ensures a finite spin moment in the ground state. Various different valencies are possible including $d^{4.5}$ in iridates with trivalent B′ [12,13], $d^{3.5}$ in ruthenates with trivalent B′ [14–16] or iridates with monovalent B′ [17], and $d^{2.5}$ in ruthenates and osmates with monovalent B′ [18,19]. Such materials have been less explored theoretically, despite the fact that their experimental magnetic response reveals several peculiarities. At high temperatures, where the mixed-valence dimers can be seen as isolated, magnetic susceptibility deviates from the conventional Curie-Weiss behavior [13,14,20,21] suggesting a nontrivial temperature evolution of the local magnetic moment. At low temperatures, interactions between the dimers become important, and signatures of frustrated magnetic behavior [16] including possible formation of a spin-liquid ground state [22] have been reported.

As we discuss in this work, even on the level of a single dimer [23–26] a variety of different local states can be realized as a function of electronic filling, dimer geometry, and spin-orbit coupling strength. Understanding the magnetic models describing interactions between such dimers first requires an understanding of the local electronic structures of an individual dimer. Here, we endeavor to obtain a microscopic insight into the electronic state and magnetism of the mixed-valence M_2O_9 dimers with different fillings $d^{4.5}$, $d^{3.5}$, and $d^{2.5}$ encountered in $4d/5d$ hexagonal perovskites. In particular, we focus on experimentally relevant details, such as the

*Corresponding author: yingli1227@xjtu.edu.cn
†Present address: Department of Physics, Indian Institute of Technology (Indian School of Mines), Dhanbad, Jharkhand, 826004, India.
‡valenti@itp.uni-frankfurt.de
§winter@physik.uni-frankfurt.de

relation between ground state and paramagnetic susceptibility. Performing exact diagonalization (ED) of dimer clusters, we find a sizable state-dependent uniaxial anisotropy of the magnetic moment and its temperature dependence, which can be employed to identify different ground states from experiment.

This paper is organized as follows. In Sec. II, we first provide a preliminary description of the local Hamiltonian for each dimer, followed by the definition of the effective magnetic moment in Sec. III. In Secs. IV to VI, we consider the ground states and behavior of the effective moment for dimers with $d^{4.5}$, $d^{3.5}$, and $d^{2.5}$ filling and in Sec. VII we present our conclusions.

II. DIMER MODEL

A. Electronic Hamiltonian per dimer

To first approximation, the hexagonal perovskites, $A_3B'M_2O_9$ crystallize in the space group $P6_3/mmc$, in which each dimer has local D_{3h} symmetry. Several compounds of the series show symmetry lowering to $C2/m$, but this structural transformation does not seem to involve electronic degrees of freedom because (i) the symmetry lowering is restricted to the octahedral rotations, while it does not change the local environment of the d-ion [22]; (ii) the symmetry lowering does not affect the metal-metal distance inside the dimer; the monoclinic (with La, Nd) and hexagonal (other $4f$'s) compounds show the common trend of the Ir-Ir distance versus ionic radius [12]. This indicates the absence of Jahn-Teller distortions [27] and a relatively minor role of vibronic effects, so that the zero-field Hamiltonian for each dimer can be written as

$$\mathcal{H}_{\rm tot} = \mathcal{H}_{\rm hop} + \mathcal{H}_{\rm CF} + \mathcal{H}_{\rm SO} + \mathcal{H}_U, \tag{1}$$

which is the sum of, respectively, the intersite hopping, on-site crystal field, spin-orbit coupling, and Coulomb interactions. We consider only the t_{2g} orbitals ($d_{xy,}$, d_{xz}, d_{yz}) on each metal atom. In this case, the later term is given by

$$\begin{aligned}\mathcal{H}_{\rm U} =& U\sum_{i,a} n_{i,a,\uparrow}n_{i,a,\downarrow} + (U'-J_H)\sum_{i,a<b,\sigma} n_{i,a,\sigma}n_{i,b,\sigma}\\ &+ U'\sum_{i,a\neq b} n_{i,a,\uparrow}n_{i,b,\downarrow} - J_H\sum_{i,a\neq b} c^\dagger_{i,a\uparrow}c_{i,a\downarrow}c^\dagger_{i,b\downarrow}c_{i,b\uparrow}\\ &+ J_H\sum_{i,a\neq b} c^\dagger_{i,a\uparrow}c^\dagger_{i,a\downarrow}c_{i,b\downarrow}c_{i,b\uparrow},\end{aligned} \tag{2}$$

where U is the on-site Coulomb repulsion, and J_H is the Hund's coupling. The labels $i, j \in \{1, 2\}$ refer to metal sites within the dimer, and $a, b \in \{xy, xz, yz\}$ refer to orbitals. Throughout, we use the approximation $U' = U - 2J_H$.

The single-particle contributions can be written in terms of the local electron creation operators $\mathbf{c}^\dagger_i \equiv (c^\dagger_{i,xy,\uparrow}\, c^\dagger_{i,xz,\uparrow}\, c^\dagger_{i,yz,\uparrow}\, c^\dagger_{i,xy,\downarrow}\, c^\dagger_{i,xz,\downarrow}\, c^\dagger_{i,yz,\downarrow})$, with the t_{2g} orbitals defined according to the local coordinates in Fig. 1(a). The local coordinates are defined in the basis of the global

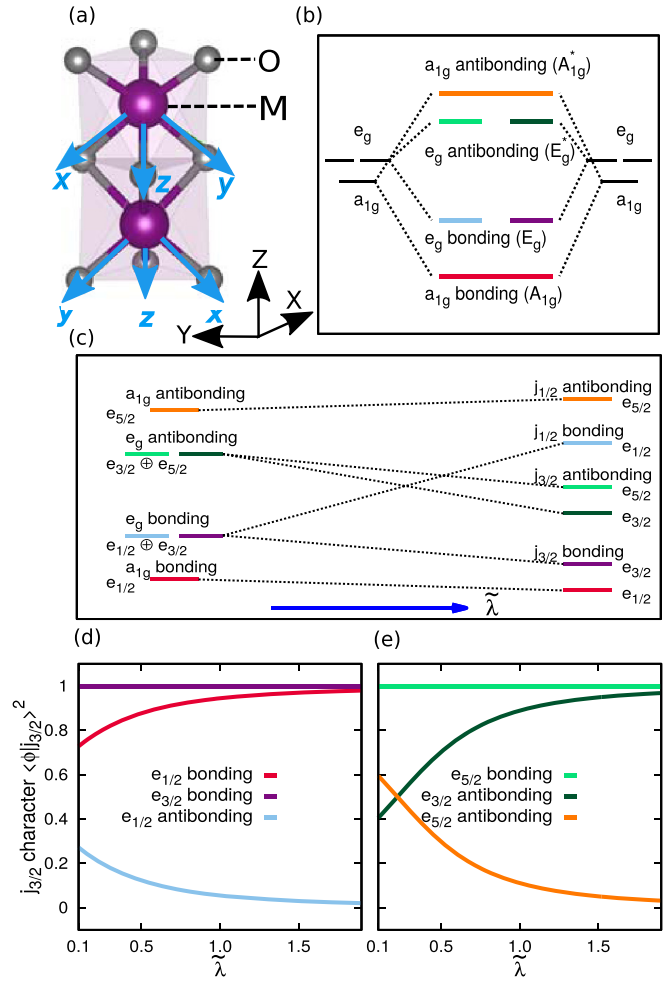

FIG. 1. (a) M_2O_9 face-shared bioctahedral dimer. Shown are the local and global coordinates. (b) Energy levels of the dimer from ED in the absence of spin-orbit coupling. (c) Energy levels-change as a function of spin-orbit coupling strength $\tilde{\lambda} = \lambda/t_2$. (d, e) Composition of $j_{3/2}$ state in terms of single-particle levels as a function of $\tilde{\lambda}$.

coordinates as

$$R_1 = \begin{pmatrix} -\sqrt{6}/6 & -\sqrt{2}/2 & -\sqrt{3}/3 \\ -\sqrt{6}/6 & \sqrt{2}/2 & -\sqrt{3}/3 \\ \sqrt{6}/3 & 0 & -\sqrt{3}/3 \end{pmatrix} \tag{3}$$

for the first atom and

$$R_2 = \begin{pmatrix} \sqrt{6}/6 & \sqrt{2}/2 & -\sqrt{3}/3 \\ \sqrt{6}/6 & -\sqrt{2}/2 & -\sqrt{3}/3 \\ -\sqrt{6}/3 & 0 & -\sqrt{3}/3 \end{pmatrix} \tag{4}$$

for the second atom. For convenience, we choose as global spin quantization axis to be the crystallographic c-axis, but employ local coordinates for the orbital definitions. The spin operator is modified as R_1S' for the first atom and R_2S' for the second atom, where S' is the standard spin operator. As a result, the spin-orbit coupling operator $\mathcal{H}_{\rm SO} = \lambda\sum_i \mathbf{L}_i \cdot \mathbf{S}_i$ has the specific form

$$\mathcal{H}_{\rm SO} = \lambda \mathbf{c}^\dagger_i (D_1 + D_2)\mathbf{c}_i, \tag{5}$$

where D_1 and D_2 are the spin-orbital matrices for the first and second atoms

$$D_1 = \begin{pmatrix} 0 & iB & -iB & 0 & A & A^* \\ -iB & 0 & iB & -A & 0 & -2iC \\ iB & -iB & 0 & -A^* & 2iC & 0 \\ 0 & -A^* & -A & 0 & -iB & iB \\ A^* & 0 & -2iC & iB & 0 & -iB \\ A & 2iC & 0 & -iB & iB & 0 \end{pmatrix}, \quad (6)$$

$$D_2 = \begin{pmatrix} 0 & iB & -iB & 0 & -A & -A^* \\ -iB & 0 & iB & A & 0 & 2iC \\ iB & -iB & 0 & A^* & -2iC & 0 \\ 0 & A^* & A & 0 & -iB & iB \\ -A^* & 0 & 2iC & iB & 0 & -iB \\ -A & -2iC & 0 & -iB & iB & 0 \end{pmatrix}, \quad (7)$$

with $A = \frac{\sqrt{2}}{4} + \frac{\sqrt{6}}{12}i$, $B = \frac{\sqrt{3}}{6}$, $C = \frac{\sqrt{6}}{12}$. Within each dimer, the local D_{3h} point group symmetry implies only two types of hopping integrals: diagonal (t_1) and off-diagonal (t_2) with respect to the t_{2g} orbitals, such that the intradimer hopping is given by

$$\mathcal{H}_{\text{hop}} = -\,\mathbf{c}_1^\dagger \begin{pmatrix} t_1 & t_2 & t_2 & 0 & 0 & 0 \\ t_2 & t_1 & t_2 & 0 & 0 & 0 \\ t_2 & t_2 & t_1 & 0 & 0 & 0 \\ 0 & 0 & 0 & t_1 & t_2 & t_2 \\ 0 & 0 & 0 & t_2 & t_1 & t_2 \\ 0 & 0 & 0 & t_2 & t_2 & t_1 \end{pmatrix} \mathbf{c}_2 + \text{H.c.} \quad (8)$$

Similarly, the crystal field is restricted to a trigonal term (Δ), given by

$$\mathcal{H}_{\text{CF}} = -\sum_{i=1}^{2} \mathbf{c}_i^\dagger \begin{pmatrix} 0 & \Delta & \Delta & 0 & 0 & 0 \\ \Delta & 0 & \Delta & 0 & 0 & 0 \\ \Delta & \Delta & 0 & 0 & 0 & 0 \\ 0 & 0 & 0 & 0 & \Delta & \Delta \\ 0 & 0 & 0 & \Delta & 0 & \Delta \\ 0 & 0 & 0 & \Delta & \Delta & 0 \end{pmatrix} \mathbf{c}_i. \quad (9)$$

Considering real materials, we expect $|t_2| = 0.2$–0.4 eV, based on density-functional theory calculations on several compounds with trivalent B′ and M = Ir, Ru using the method described in Refs. [28,29]. For 4d elements such as Ru and Rh, we expect $U = 2.5$–3.5 eV and $\lambda = 0.1$–0.2 eV [30]. In contrast, for 5d elements such as Os and Ir, we expect $U = 1.5$–2.0 eV and $\lambda = 0.3$–0.4 eV [31]. Throughout, we use the reduced values $\tilde{U} = U/t_2$, $\tilde{\lambda} = \lambda/t_2$, $\tilde{t_1} = t_1/t_2$, $\tilde{\Delta} = \Delta/t_2$ and fix the ratio of $J_H/U = 0.18$ for simplicity. Throughout the text, we use lower-case quantities to characterize the single-particle levels, and upper-case quantities to label the many-body states.

B. Single-particle levels

We can understand some aspects of the many-body phase diagram by considering the $\tilde{U} \to 0$ limit. Therefore we first consider the evolution of the single-particle energy levels assuming each dimer has D_{3h} point-group symmetry, as described above. In the absence of spin-orbit coupling (SOC), the local trigonal crystal field weakly splits the t_{2g} orbitals into singly degenerate a_{1g} $[\frac{1}{\sqrt{3}}(d_{xy} + d_{xz} + d_{yz})]$ and doubly degenerate e_g $[\frac{1}{\sqrt{3}}(d_{xy} + e^{\frac{2\pi i}{3}} d_{xz} + e^{-\frac{2\pi i}{3}} d_{yz})$, $\frac{1}{\sqrt{3}}(d_{xy} + e^{-\frac{2\pi i}{3}} d_{xz} + e^{\frac{2\pi i}{3}} d_{yz})]$. By convention, we label such atomic combinations according to their representation in D_{3h}, which describes a single trigonally distorted MO_6 octahedron. For $\Delta > 0$, the a_{1g} levels lie below the e_g levels, as depicted in Fig. 1. The intradimer hopping is purely diagonal in this atomic basis, with $t_{a_{1g}} = t_1 + 2t_2$ and $t_{e_g} = t_1 - t_2$. In the absence of SOC, these hoppings lead to the formation of bonding and antibonding combinations of atomic a_{1g} and e_g orbitals. Figure 1(b) shows the ordering of such levels for physically relevant parameters, $t_2 > 0$ and $t_2 \gg |t_1|$.

The inclusion of SOC leads to the splitting of the single-particle levels. In the limit of strong SOC ($\lambda \gg \Delta, t_1, t_2$), the local atomic states are more conveniently described in terms of doublet $j_{1/2}$ (with the spin, orbital, and total effective angular momentum as $S = \frac{1}{2}, L_{\text{eff}} = 1, J_{\text{eff}} = \frac{1}{2}$, respectively) and quadruplet $j_{3/2}$ ($S = \frac{1}{2}, L_{\text{eff}} = 1, J_{\text{eff}} = \frac{3}{2}$) levels. Intradimer hopping is not diagonal with respect to the $j_{1/2}/j_{3/2}$ character, and therefore leads to *both* the mixing of the j-states and the formation of bonding/antibonding combinations. Formally, the mixed spin-orbitals at intermediate $\tilde{\lambda}$ can be labelled according to their double group representation within D_{3h}, which admits three Kramers doublet representations: $e_{1/2}$, $e_{3/2}$, and $e_{5/2}$, as shown in Fig. 1(c). A character table for these states is given in the Appendix A. Of these single-particle levels, the $e_{3/2}$ states have pure $j_{3/2}$ character, while the $e_{1/2}$ and $e_{5/2}$ states are mixtures of atomic $j_{1/2}$ and $j_{3/2}$ functions. As an example of the relation between the atomic relativistic $j_{1/2}$ / $j_{3/2}$ basis and the three Kramers doublets, in Figs. 1(d) and 1(e) we display the weights $\langle\phi|j_{3/2}\rangle^2$ of $j_{3/2}$ states in terms of the three Kramers doublets $e_{1/2}$, $e_{3/2}$, and $e_{5/2}(|\phi\rangle$ states) as a function of $\tilde{\lambda}$. In the nonrelativistic limit $\tilde{\lambda} = 0$, the states are distributed to all relativistic states. With increasing $\tilde{\lambda}$, the contribution to $j_{3/2}$ of the lowest bonding states $e_{1/2}$ and $e_{3/2}$ arises and finally these states become pure $j_{3/2}$ while the highest antibonding state $e_{1/2}$ is finally a $j_{1/2}$ state, as it is the antibonding $e_{5/2}$. In contrast, bonding $e_{5/2}$ shows a nonmonotonous composition of $j_{3/2}$ and $j_{1/2}$ with $\tilde{\lambda}$.

As a function of SOC strength $\tilde{\lambda}$, the ordering of the single-particle levels changes, such that the ground state of a single dimer is sensitive to both $\tilde{\lambda}$ and filling. For intermediate values of $\tilde{\lambda}$ found in real materials, this also has the effect of confining the $j_{1/2}$ bonding and $j_{3/2}$ antibonding levels into a narrow energy range, which significantly reduces the energy scales relevant to the magnetic response of the dimer. The consequences for specific fillings are considered in Secs. IV to VI with the inclusion of Coulomb interactions.

III. DEFINITION OF EFFECTIVE MOMENTS

Given that we are interested in dimers with open-shell (e.g., doublet) ground states, it is useful to characterize them according to their magnetic response. For isolated magnetic ions or dimers, it is conventional to describe the molar magnetic susceptibility in terms of temperature-dependent effective moments $\mu_{\text{eff}}^{\alpha}(T)$, defined by

$$\chi^{\alpha}(T) = \frac{N_A}{3k_B T}\left[\mu_{\text{eff}}^{\alpha}(T)\right]^2, \quad (10)$$

where $\alpha \in \{x, y, z\}$. In simple cases where there are no low-lying excited multiplets, and the ground state is a pure spin multiplet (there is no orbital degeneracy, and spin-orbit coupling can be neglected), then the susceptibility should follow a pure Curie law, with $\mu_{\rm eff} = g_S\sqrt{S(S+1)}$ being temperature-independent and isotropic. However, when any of these conditions are violated, as it is common in real materials with strong SOC, the susceptibility of isolated magnetic species will generally be a more complex function of temperature.

Additional non-Curie contributions to $\chi(T)$ occur, essentially, from two sources. First, there can exist low-lying excited multiplets that become thermally populated at relevant temperatures. Second, when spin-orbit coupling is relevant, it is important to note that the SOC operator $\mathcal{H}_{\rm SO} = \lambda \mathbf{L}\cdot\mathbf{S}$ generally does not commute with the Zeeman operator, given by $\mathcal{H}_Z = \mu_B \mathbf{H}\cdot\mathbf{M}$, with $\mathbf{M} = (g_S\mathbf{S} + g_L\mathbf{L})$. As a result, the magnetic field induces mixing between different multiplets, introducing additional terms in the susceptibility analogous to the phenomenon of van Vleck paramagnetism. These effects are well documented, and have been studied for isolated ions both theoretically and experimentally [32]. While it is clear that exchange couplings $\sim J$ between magnetic species further impact the paramagnetic susceptibility, provided the temperature is sufficiently large $T \gg J$, then $\chi(T)$ should generally be dominated by local single-species effects. As a result, the behavior of $\mu^{\alpha}_{\rm eff}(T)$ represents a first clue regarding the nature of the local electronic ground state. We focus on this quantity in the following sections.

IV. $d^{4.5}$ FILLING

A. Survey of materials

We first consider the case of $d^{4.5}$ filling that corresponds to three holes per dimer. This filling can be found in $A_3B'M_2O_9$ with trivalent B′ and M = Rh or Ir, among which mostly the iridates have been studied experimentally. All of them show strong deviations from the Curie-Weiss behavior and develop a characteristic bend in the inverse susceptibility at 50–100 K [13]. The linear fit to the high-temperature part returns the effective moments of 1.53 μ_B/f.u. (B′ = In) and 1.79 μ_B/f.u. (B′ = Sc) that were interpreted as the $S = \frac{1}{2}$ state of the mixed-valence dimer [13], although very high Curie-Weiss temperatures of several hundred Kelvin put into question the validity of such a fit. Below the bend, a much lower effective moment of 0.76 μ_B/f.u. (B′ = In) is obtained [22], and a magnetic entropy on the order of $R\ln 2$ is released [12,13,22], suggesting the ground-state doublet of a hitherto unknown nature.

At even lower temperatures, interactions between the dimers come into play. $Ba_3YIr_2O_9$ undergoes long-range magnetic ordering at 4.5 K [33,34], whereas $Ba_3InIr_2O_9$ reveals persistent spin dynamics down to at least 20 mK, with local probes suggesting a collective, possibly spin-liquid behavior of local moments below 1 K [22]. $Ba_3ScIr_2O_9$ does not show long-range magnetic order down to at least 2 K, but pends experimental characterization at lower temperatures [33].

Rh atoms can also be accommodated in the 6*H* perovskite structure, but show strong site mixing with the B′ atoms [11,35]. Therefore, no experimental information on the magnetism of pure Rh_2O_9 dimers is presently available.

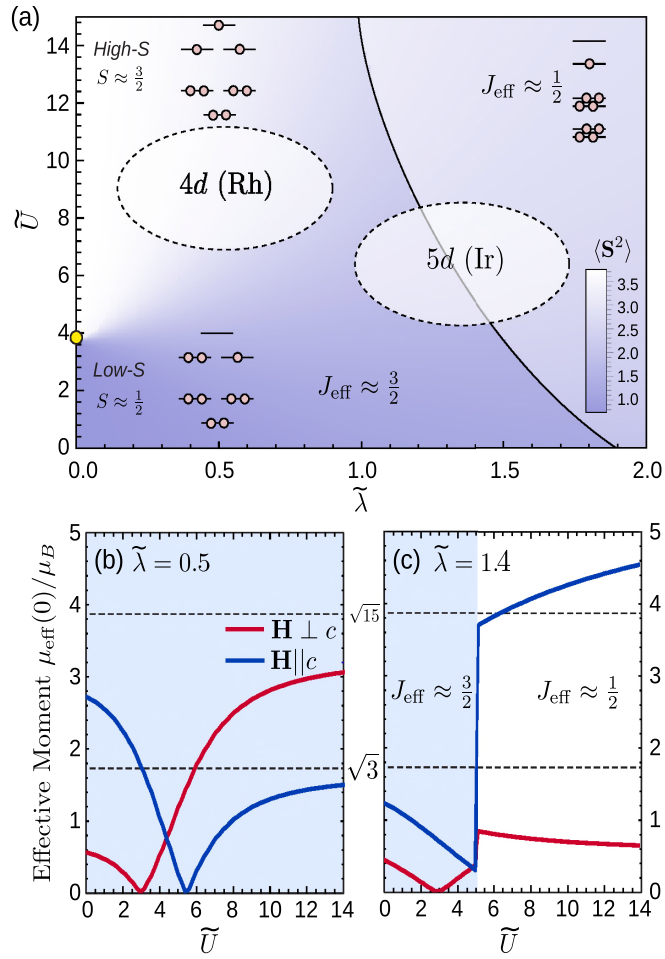

FIG. 2. (a) Phase diagram of theoretical ground state of a $d^{4.5}$ dimer as a function of $\tilde{U} = U/t_2$ and $\tilde{\lambda} = \lambda/t_2$ for $t_1 = \Delta = 0$. We fix $J_H/U = 0.18$. (b, c) Evolution of the zero-temperature effective moment [Eq. (10)] for $\tilde{\lambda}$ values corresponding to 4*d* and 5*d* materials, respectively.

B. Phase diagram

The theoretical ground state of a $d^{4.5}$ dimer as a function of $\tilde{U}$ and $\tilde{\lambda}$ is shown in Fig. 2(a) for $t_1 = \Delta = 0$. The color shading indicates the expectation value of the total spin moment squared $\langle \hat{\mathbf{S}}^2 \rangle$ per dimer. In the nonrelativistic limit $\tilde{\lambda} \to 0$, there are two possible ground states depending on the relative strength of $\tilde{t}_1$ and $\tilde{U}$ (and J_H/t_2 since we fix the ratio $J_H/U = 0.18$). If the Hund's coupling is large compared to the splitting of the antibonding e_g and a_{1g} levels ($J_H \gg t_2$), the ground state is a high-spin $S = 3/2$ quartet with nominally one hole in each of the antibonding $e_{3/2}$, and $e_{5/2}$ orbitals [Fig. 2(a) upper left corner]. In this configuration, the orbital angular momentum is completely quenched, and $\langle \hat{\mathbf{S}}^2 \rangle = S(S+1) = 15/4$. In contrast, for $J_H \ll t_2$, a low-spin $S = 1/2$ configuration is instead preferred, with two holes nominally occupying the a_{1g} antibonding state, and one hole occupying the e_g antibonding state [lower left corner in Fig. 2(a)]. This is indicated by

$\langle \hat{\mathbf{S}}^2 \rangle = 3/4$. Provided C_3 rotational symmetry is preserved, this later configuration has unquenched orbital angular momentum, as the e_g hole may occupy either the $e_{3/2}$ or $e_{5/2}$ single-particle levels shown in Fig. 1(c). The combined spin and orbital degrees of freedom provide an overall four-fold ground-state degeneracy for $\tilde{\lambda} = 0$. As the partially occupied single-particle levels are predominantly of $j_{3/2}$ character, we refer to this ground state as having total $J_{\text{eff}} \approx 3/2$.

For both the high-spin $S \approx 3/2$ and low-spin $J_{\text{eff}} \approx 3/2$ cases, introducing small $\tilde{\lambda}$ leads to a splitting of the quartet states into pairs of Kramers doublets. In the high-spin limit, this can be viewed as the introduction of an on-site zero-field splitting term $(S_x^2 + S_y^2 + S_z^2)$ that energetically prefers the $m_S = \pm 1/2$ states. In the low-spin limit, SOC leads to spin-orbital locking of the unquenched L and S moments, stabilizing the $m_J = \pm 1/2$ states. With finite $\tilde{\lambda}$, these cases are smoothly connected, such that there is no sharp "phase transition" for small $\tilde{\lambda}$ on increasing $\tilde{U}$. As indicated in Fig. 2(a), $\langle \hat{\mathbf{S}}^2 \rangle$ evolves continuously between the high-spin and low-spin limits, as S is no longer a good quantum number with finite SOC.

Further increasing $\tilde{\lambda}$ leads to a change in the ordering of the single-particle $e_{1/2}$ bonding and $e_{5/2}$ antibonding levels, as discussed in Sec. II B. This stabilizes a different "low-spin" $J_{\text{eff}} \approx 1/2$ ground state, with nominally two holes in the antibonding $j_{1/2}$ level ($e_{5/2}$), and one hole in the bonding $j_{1/2}$ level ($e_{1/2}$).

Considering real materials, hypothetical Rh-based dimers should fall well within the high-spin $S \approx 3/2$ region. In contrast, Ir-based dimers may lie on the border of the $J_{\text{eff}} \approx 1/2$ and $J_{\text{eff}} \approx 3/2$ regions if microscopic parameters determined by resonant inelastic x-ray scattering (RIXS) on integer-valence Ir_2O_9 dimers [10,36] are used. Similar experiments on the mixed-valence compounds would be required to identify the experimental ground states of real materials. In this context, a useful observation is that the different electronic configurations of the dimers can also be distinguished by the anisotropy and magnitude of the effective magnetic moments $\mu^{\alpha}_{\text{eff}}(T)$, as defined in Sec. III.

In Fig. 2(b) we show the evolution of the zero-temperature limit of the effective moment per dimer $\mu_{\text{eff}}(0)$ as a function of $\tilde{U}$ for $\tilde{\lambda} = 0.5$, corresponding to the expected range for $4d$ dimers of Rh. In this case, SOC reduces the average value of $\mu_{\text{eff}}(0)$ to well below the spin-only value of $\sqrt{15}$ for pure $S = 3/2$ moments for all values of $\tilde{U}$. The crossover from the low-spin to high-spin ground state with increasing $\tilde{U}$ leads to a reversal of the anisotropy of the effective moment; for small $\tilde{U}$, $\mu^{ab}_{\text{eff}} < \mu^{c}_{\text{eff}}$, while for large $\tilde{U}$, $\mu^{ab}_{\text{eff}} > \mu^{c}_{\text{eff}}$. We expect that hypothetical Rh-based dimers should fall into the later category.

In the region of parameters applicable to Ir-based dimers [$\tilde{\lambda} = 1.4$; Fig. 2(c)], increasing $\tilde{U}$ leads to a phase transition from a $J_{\text{eff}} \approx 3/2$ to $J_{\text{eff}} \approx 1/2$ ground state, which is marked by a significant increase of the average effective moment. The average moment in the $J_{\text{eff}} \approx 3/2$ state is strongly suppressed by SOC, and displays an anisotropy that is strongly sensitive to various parameters such as $\tilde{\lambda}$, $\tilde{U}$, $\tilde{\Delta}$, and $\tilde{t}_1$. The influence of the later two parameters is shown in Figs. 3(a) and 3(b). Modifying $\tilde{\Delta}$ and $\tilde{t}_1$ can lead to reversals of the anisotropy of the effective moment in the $J_{\text{eff}} \approx 3/2$ region. Greatly increasing $\tilde{t}_1$ also stabilizes the $J_{\text{eff}} \approx 1/2$ ground state, ultimately driving the phase transition. The $J_{\text{eff}} \approx 1/2$ ground state at large $\tilde{U}$ and/or $\tilde{t}_1$ is characterized by a much larger average moment, which is strongly anisotropic with $\mu^{c}_{\text{eff}} > \mu^{ab}_{\text{eff}}$. As shown in Figs. 3(c) and 3(d), this anisotropy is only weakly affected by crystal field $\tilde{\Delta}$, and remains for a wide range of values of $\tilde{t}_1$ hopping.

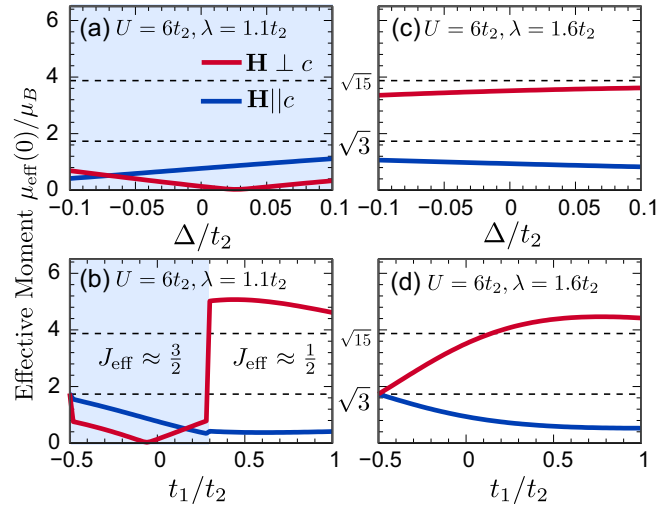

FIG. 3. Evolution of the zero-temperature effective moment [Eq. (10)] as a function of $\tilde{\Delta} = \Delta/t_2$ and $\tilde{t}_1 = t_1/t_2$.

C. Comparison to experiment

For temperatures large compared to the interactions between dimers, the effective moment per dimer can be extracted from experimental susceptibility data χ^{α} via

$$\mu^{\alpha}_{\text{eff}}(T) \approx \sqrt{\frac{3k_B T}{N_A}\chi^{\alpha}_{\text{exp}}(T)}, \tag{11}$$

where α indicates the field direction, N_A is the Avogadro constant, k_B is the Boltzmann constant, and T is the temperature. Given that all Ir-based $d^{4.5}$ dimers discussed above show features in the specific heat at low temperatures $T \lesssim 10\,\text{K}$ that account for a significant fraction of $R\ln 2$ entropy, we assume that the magnetic couplings between dimers are relatively weak. As a result, the temperature dependence of $\chi(T)$ above room temperature should be largely dominated by the evolution of $\mu^{\alpha}_{\text{eff}}(T)$. In Figs. 4(a) to 4(c), we thus show the theoretical temperature dependence of the effective moment for selected parameters corresponding to regions expected for real materials. For real materials, $|t_2| = 0.2$–$0.4\,\text{eV}$, such that room temperature corresponds to roughly $\tilde{T} = T/t_2 \sim 0.1$.

For hypothetical Rh-based dimers [Fig. 4(a)], we find that thermal fluctuations rapidly overcome the "single-dimer" spin-anisotropy from SOC, restoring the spin-only value of $\sqrt{15}\,\mu_B$ as temperature is raised. Nevertheless, below room temperature such materials will display strong deviations from Curie behavior even in the absence of interdimer couplings. The green area above 0.047 is the region where the first excited state is occupied.

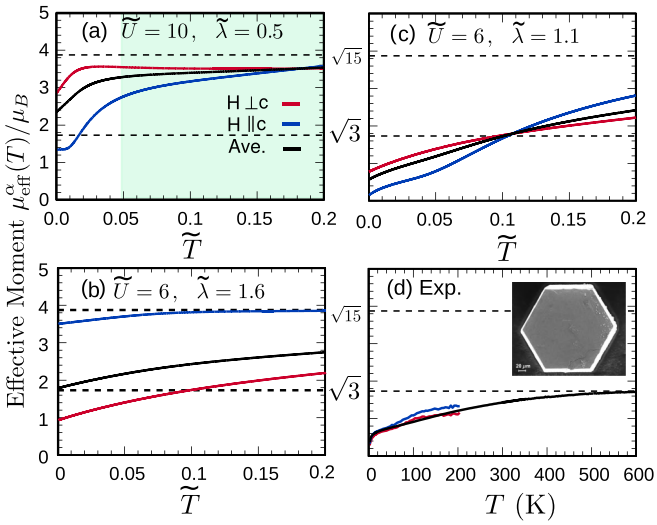

FIG. 4. Temperature dependence of the magnetic moments for $d^{4.5}$ dimers for various $\tilde{U}(U/t_2)$ and $\tilde{\lambda}(\lambda/t_2)$ values for $t_1 = \Delta = 0$. (a) Parameters relevant for isolated $4d$ dimers. The green area displays the region where the first excited state is occupied. (b, c) Parameters relevant for isolated $5d$ dimers in $J_{\rm eff} \approx 1/2$ and $J_{\rm eff} \approx 3/2$ ground states, respectively. The energy of the first excited state is above 0.2 t_2. (d) Experimental effective moment for $Ba_3InIr_2O_9$ derived from both single-crystal and powder measurements. The insert of Fig. 4(d) is the scanning electron microscopy image of the $Ba_3InIr_2O_9$ crystal.

For Ir-based dimers, we consider $\tilde{\lambda} = 1.1$ and 1.6 corresponding to the $J_{\rm eff} \approx 3/2$ and $J_{\rm eff} \approx 1/2$ ground states, respectively [Figs. 4(b) and 4(c)]. In both cases, $\mu_{\rm eff}(T)$ is a monotonically increasing function. The energy of the first excited state is above 0.2 t_2. For the $J_{\rm eff} \approx 1/2$ ground state [Fig. 4(c)], the effective moment is strongly anisotropic, with an average value that exceeds the value of $\sqrt{3}$ expected for pure $J_{\rm eff} = 1/2$ states. A similar effect is known for isolated ions with $J_{\rm eff} = 1/2$ ground states [32], and therefore is not unique to the dimer case. In contrast, the anisotropy is expected to be weaker in the $J_{\rm eff} = 3/2$ ground state [Fig. 4(b)], with average values below $\sqrt{3}$ at experimentally relevant temperatures.

Our results suggest that the presence or absence of this anisotropy can be used to diagnose the electronic ground state of mixed-valence dimers. Unfortunately, this anisotropy aspect remains unexplored, as most of the experimental data reported so far have been measured on powders, with no single crystals available. We could overcome this problem by growing a small single crystal of $Ba_3InIr_2O_9$ (see Appendix B for details of crystal growth and characterization) and measured its magnetic susceptibility along different directions. Data up to 200 K were obtained, while at higher temperatures the signal drops below the sensitivity threshold of the magnetometer, but already these data indicate weak anisotropy of the paramagnetic response. The effective moment is quite low and approaches $\sqrt{3}$ at elevated temperatures. These observations strongly suggest that the ground state of the mixed-valence dimer in $Ba_3InIr_2O_9$ is $J_{\rm eff} = 3/2$. A similar $J_{\rm eff} = 3/2$ scenario can be envisaged for other mixed-valence iridates with trivalent B′, where the susceptibility data around room temperature also yield effective moments of about $\sqrt{3}$ [13].

An ideal $J = 3/2$ state is a quartet with zero magnetic dipole moment, but under experimental conditions it will usually split into two Kramers doublets, which is also the case here at $\tilde{\lambda} \neq 0$. This explains why at low temperatures magnetic entropy of not more than $R \ln 2$ is recovered [12,22,33], corresponding to the lower Kramers doublet. Low-temperature magnetism associated with this doublet should be then treated as an effective spin-$\frac{1}{2}$ with a strongly renormalized g-tensor. The very low g-value elucidates the fact that magnetization of $Ba_3InIr_2O_9$ does not reach saturation even at 14 T, even though exchange couplings are on the order of several Kelvin and would be easily saturated in a conventional spin-$\frac{1}{2}$ antiferromagnet with $g = 2.0$ [22].

V. $d^{3.5}$ FILLING

A. Survey of materials

Materials with $d^{3.5}$ filling are found for two different compositions $A_3B'M_2O_9$. The first case corresponds to M being a group 8 element (Os, Ru) and trivalent B′, whereas the second case corresponds to M being a group 9 element (Ir, Rh) and monovalent B′.

The mixed-valence ruthenates have been reported for a wide range of trivalent B′ ions, including Y, In, and many of the lanthanides. All these compounds show strong deviations from the Curie-Weiss behavior [14,20,37]. An effective spin-$\frac{1}{2}$ state was conjectured [16] for $Ba_3B'Ru_2O_9$ with B′ = In, Y, Lu from the relatively low values of the magnetic susceptibility and from the local moment of 1.0 μ_B/dimer in the magnetically ordered state of $Ba_3YRu_2O_9$ [15]. On the other hand, $Ba_3LaRu_2O_9$ shows an overall higher susceptibility that approaches the Curie-Weiss regime for spin-$\frac{3}{2}$ above room temperature [38]. The local moment of 2.6–2.8 μ_B/dimer in the magnetically ordered state [15,38] also supports the spin-$\frac{3}{2}$ scenario. These dissimilar trends indicate the presence of at least two competing electronic states in the $d^{3.5}$ Ru_2O_9 dimers. Indeed, local excitations of magnetic origin were observed by inelastic neutron scattering around 35 meV and assigned to a transition between these states tentatively identified as $S = 1/2$ and $S = 3/2$ states of the mixed-valence dimer [16,38].

Similar to the $d^{4.5}$ iridates, the $d^{3.5}$ ruthenates exhibit a range of magnetic ground states, from long-range order confirmed in B′ = La, Nd, Y [15,37,38] and anticipated for B′ = Lu [16], to a static disordered state in $Ba_3InRu_2O_9$ [16]. To our knowledge, Os-based dimers with $d^{3.5}$ filling have yet to be explored.

Examples of the second case of materials include $Ba_3(Na/Li)Ir_2O_9$ [17,39]. Susceptibility measurements show signs of magnetic order at 75 and 50 K for B′ = Li and Na, respectively [17]. Curie-Weiss fits of the magnetic susceptibility between about 150 K and room temperature return the effective moments of 3.93 μ_B/f.u. (B′ = Li) and 3.60 μ_B/f.u. (B′ = Na) [17]. On the other hand, Curie-Weiss temperatures of, respectively, −576 K and −232 K suggest that a true paramagnetic regime may not have been reached in this

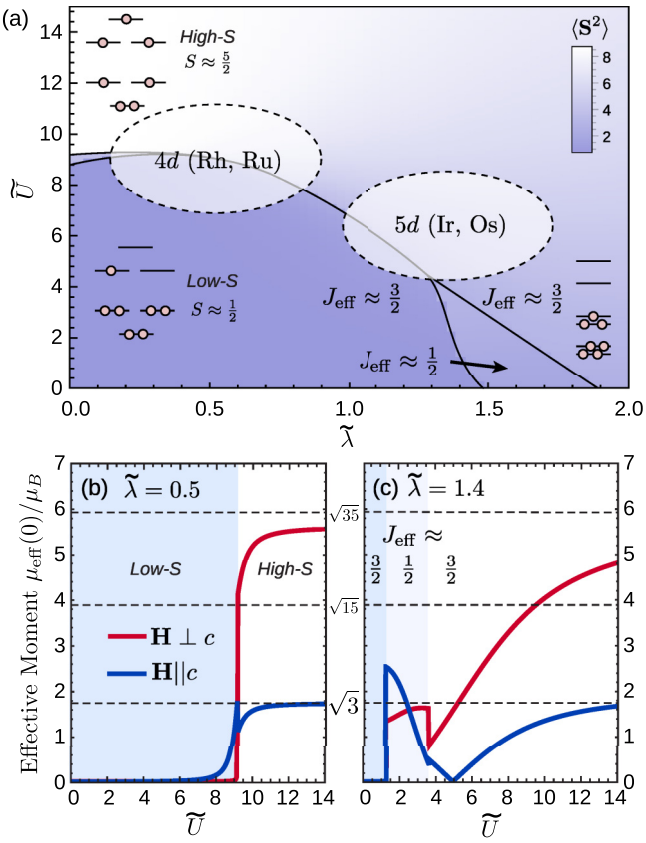

FIG. 5. (a) Phase diagram of theoretical ground state of a $d^{3.5}$ dimer as a function of $\tilde{U} = U/t_2$ and $\tilde{\lambda} = \lambda/t_2$ for $t_1 = \Delta = 0$. We fix $J_H/U = 0.18$. (b, c) Evolution of the zero-temperature effective moment as a function of $\tilde{U}$ for $\tilde{\lambda}$ values corresponding to $4d$ and $5d$ materials, respectively. Note that the jumps in the figures are due to changes in $J_{\rm eff}$.

temperature range. To our knowledge, Rh-based dimers with $d^{3.5}$ filling were not reported.

B. Phase diagram

The theoretical ground state of a $d^{3.5}$ dimer as a function of $\tilde{U}$ and $\tilde{\lambda}$ is shown in Fig. 5(a) for $t_1 = \Delta = 0$. Similar to the $d^{4.5}$ case, the nonrelativistic limit $\tilde{\lambda} \to 0$ features high-spin and low-spin states, which are stabilized for large and small J_H/t_2, respectively. Large Hund's coupling produces a high-spin $S = 5/2$ state with nominally one hole in each of the antibonding $e_{3/2}$, $e_{5/2}$ and bonding $e_{1/2}$, $e_{3/2}$ orbitals. In this state, the orbital angular momentum is essentially quenched. In contrast, weak interactions lead to a low-spin $S = 1/2$ ground state, with two holes nominally occupying the a_{1g} antibonding level, and three holes occupying the e_g antibonding levels. This low-spin ground state has orbital degeneracy associated with the single electron in the e_g antibonding levels implying an unquenched orbital moment. In the nonrelativistic limit, the ground state is four-fold degenerate, with unpaired electrons occupying single-particle levels with predominant $j_{3/2}$ character. As a result, we refer to this low-spin ground state as $J_{\rm eff} \approx 3/2$. A very narrow intermediate-spin $S \approx 3/2$ phase may also lie between these cases for weak SOC.

In contrast to the $d^{4.5}$ case, a distinct transition occurs between the low-spin and high-spin states, as can be seen in $\mu_{\rm eff}(0)$ as a function of $\tilde{U}$, shown in Fig. 5(b) for $\tilde{\lambda} = 0.5$. The introduction of small $\tilde{\lambda}$ leads to spin-orbital locking in the low-spin phase, which ultimately quenches completely the effective moment. As a result, $\mu_{\rm eff}(0) \approx 0$ for small $\tilde{U}$. From the perspective of the single-particle levels, the unpaired electron occupies an $e_{3/2}$ level, which has pure $j_{3/2}$ character. As a result, the effective moment is precisely zero. For the high-spin case, small λ leads to a splitting of the six degenerate $S = 5/2$ states into three pairs of Kramers doublets. The $m_S = \pm 1/2$ doublet forms the ground state, which leads to $\mu^{ab}_{\rm eff} > \mu^{c}_{\rm eff} \approx \sqrt{3}$. Considering real materials, we anticipate that Rh- and Ru-based dimers may lie in an interesting region on the border of the high-spin and low-spin states.

Returning back to the phase diagram Fig. 5(a), we can also consider the sequence of ground states that occur for weak interactions as a function of $\tilde{\lambda}$. These can be understood in the single particle picture from Fig. 1(c). As noted above, for small $\tilde{\lambda}$, the $J_{\rm eff} \approx 3/2$ ground state has a single electron occupying an e_g antibonding level of $e_{3/2}$ symmetry, with pure $j_{3/2}$ antibonding character. With increasing $\tilde{\lambda}$, this level crosses the $j_{1/2}$ bonding level of $e_{1/2}$ symmetry, leading instead to a ground state with $J_{\rm eff} \approx 1/2$ nature. Finally, further increasing $\tilde{\lambda}$ leads to another crossing of the $e_{1/2}$ level with an $e_{5/2}$ level that is nominally $j_{3/2}$ antibonding. As a result, the ground state in the $\tilde{\lambda} \to \infty$ limit consists of two holes in the antibonding $j_{1/2}$ level ($e_{5/2}$), two holes in the bonding $j_{1/2}$ level ($e_{1/2}$), and one hole in the antibonding $j_{3/2}$ level ($e_{5/2}$). This later $J_{\rm eff} \approx 3/2$ ground state is smoothly connected to the high-spin $S = 5/2$ state appearing at weak SOC.

In Fig. 5(c), we show the evolution of the zero-temperature effective moment as a function of $\tilde{U}$ for $\tilde{\lambda} = 1.4$, corresponding to $5d$ materials. In this case, $\mu_{\rm eff}(0)$ can be used to distinguish the three different ground states. For small $\tilde{U}$, the effective moment is 0, as the low-energy degrees of freedom have pure $J_{\rm eff} \approx 3/2$ character. When entering into the $J_{\rm eff} \approx 1/2$ state upon increasing $\tilde{U}$, the effective moment jumps to an average value $\sim\sqrt{3}\mu_B$. With further increasing U, the average effective moment again drops when entering the $J_{\rm eff} \approx 3/2$ ground state. However, interactions ultimately enhance the spin contribution to the moment, such that $\mu_{\rm eff}$ tends to grow with increasing U, J_H. The anisotropy $\mu^{ab}_{\rm eff} > \mu^{c}_{\rm eff}$ is maintained throughout this later $J_{\rm eff} \approx 3/2$ phase.

C. Comparison to experiment

In Fig. 6, we show the temperature dependence of the effective moment for selected parameters corresponding to regions expected for real materials. For Ru/Rh systems, we consider $\tilde{\lambda} = 0.5$, with $\Delta = t_1 = 0$ for simplicity. Figures 6(a) and 6(b) show the expected behavior for the high-spin and low-spin ground states, respectively. The green areas display the regions where the lowest excited states are sequentially filled as a function of temperature. For the high-spin state, we find a strong temperature dependence as thermal fluctuations rapidly overwhelm the local "single-ion" magnetic anisotropies. Thus the anisotropy of the effective moment

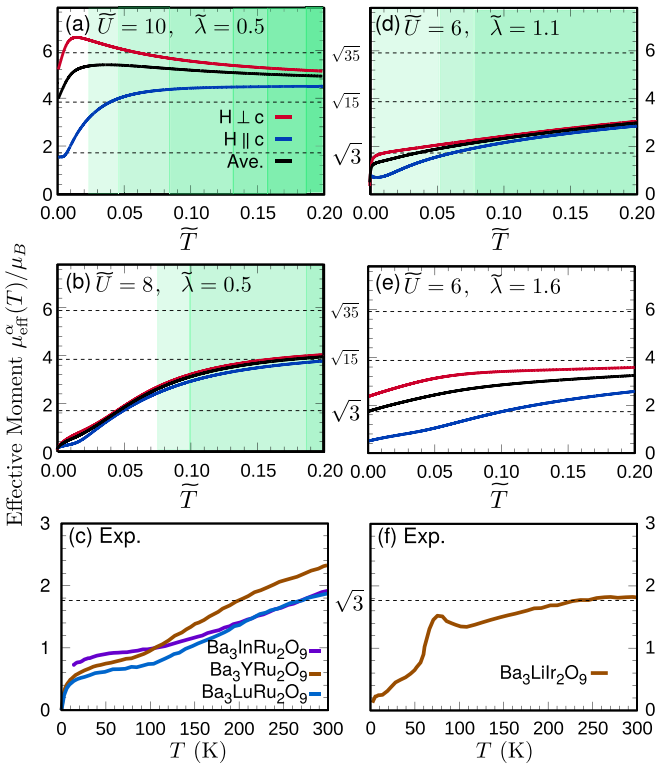

FIG. 6. Temperature dependence of the magnetic moments for $d^{3.5}$ dimers with various $\tilde{U}$ and $\tilde{\lambda}$ values for $t_1 = \Delta = 0$. (a, b) Theoretical results for isolated $4d$ dimers in high-spin and low-spin ground states, respectively. The green areas display the regions where the six lowest excited states are filled sequentially. (c) Experimental effective moment for various Ru-based dimers based on data from Ref. [16]. (d, e) Theoretical results for isolated $5d$ dimers in different $J_{\rm eff} \approx 3/2$ ground states. The green areas in (d) display the regions where the three lowest excited states are filled sequentially. The energy of the first excited state in (e) is above $0.2\,t_2$. (f) Experimental effective moment for $Ba_3LiIr_2O_9$ derived from Ref. [17].

is suppressed with increasing T, and the average value becomes comparable to the pure spin value of $\sqrt{35}\mu_B$ for $S = 5/2$. For the low-spin state, $\mu^{\alpha}_{\rm eff}(T)$ is nearly isotropic at all temperatures, and slowly decreases to zero as the temperature is lowered. Considering real materials, Fig. 6(b) closely resembles the response of the powder samples of $Ba_3YRu_2O_9$, $Ba_3LuRu_2O_9$, and $Ba_3InRu_2O_9$ reported in Refs. [14,16]. Moreover, magnetic susceptibility measured on a single crystal of $Ba_3InRu_2O_9$ shows a nearly isotropic magnetic response [20], in agreement with the low-spin scenario. In Fig. 6(c), we plot the $\sqrt{(3k_BT/N_A)\chi_{\rm avg}(T)}$ for all three compounds, derived from the experimental $\chi(T)$ in Ref. [16]. As above, we expect $|t_2| = 0.2$–0.3 eV, so room temperature corresponds to roughly $\tilde{T} = T/t_2 \sim 0.1$.

Given this correspondence, we can conclude that the Ru-based dimers very likely have low-spin ground states. Similar to the $d^{4.5}$ iridates, this $J_{\rm eff} = 3/2$ state is represented by two Kramers doublets. We emphasize that the suppression of $\mu_{\rm eff}(T)$ at low temperatures results from SOC, which couples the $S = 1/2$ moment per dimer with the unquenched orbital moment such that the total effective moment is nearly canceled in the ground state. This scenario is also compatible with the relatively small ordered moments deduced from neutron scattering [15], and with the observed electronic excitation around 35 meV [16] that should be assigned to the transition between the two doublets.

An interesting exception to this picture is the behavior of $Ba_3LuRu_2O_9$, which shows a larger average $\mu_{\rm eff}$ over an extended temperature range. It may be possible that this material adopts a high-spin or intermediate-spin ground state instead; a nontrivial test of this scenario would be demonstration of significant anisotropy of $\mu^{\alpha}_{\rm eff}(T)$, with $\mu^{ab}_{\rm eff} > \mu^{c}_{\rm eff}$, if single crystal samples become available.

For Ir- and Os-based dimers, the two realistic ground states are both described as $J_{\rm eff} \approx 3/2$. As a result, they are less distinguishable on the basis of magnetic susceptibility. In Figs. 6(d) and 6(e), we compare $\mu_{\rm eff}(T)$ for $\tilde{U} = 6$ and different values of $\tilde{\lambda} = 1.1,\ 1.6$ corresponding to the two ground states. The green areas in In Fig. 6(d) display the regions where the lowest three excited states are filled as a function of temperature. The energy of the first excited state is above $0.2\ t_2$ in Fig. 6(e). In both cases, we find $\mu^{ab}_{\rm eff} > \mu^{c}_{\rm eff}$, with average values falling in similar ranges. In Fig. 6(f), we plot $\sqrt{(3k_BT/N_A)\chi_{\rm avg}(T)}$ for $Ba_3LiIr_2O_9$, derived from the experimental susceptibility from Ref. [17]. The experimental value of $\sim 2\mu_B$ around room temperature is compatible with the theoretical results in Fig. 6(d) at $\tilde{T} = 0.1$. On the other hand, the effective moments of 3.60 and 3.93 μ_B/f.u. obtained from the Curie-Weiss fits [17] are comparable to the high-temperature limit in Fig. 6(e). A general problem here is that relatively high magnetic ordering temperatures of 50 and 75 K indicate sizable exchange interactions between the dimers. Therefore, it may be difficult to directly compare the theoretical and experimental data within the available temperature range.

VI. $d^{2.5}$ FILLING

A. Survey of materials

Materials with $d^{2.5}$ filling have $A_3B'M_2O_9$ compositions with monovalent B′ and transition metal M belonging to group 8 (Os, Ru). Of these, $Ba_3NaRu_2O_9$ shows a rather abrupt decrease [18] in the magnetic susceptibility at 210 K, which is accompanied by a structural transition and interdimer charge order [40]. The low-temperature phase is thus composed of distinct $(Ru^{6+})_2O_9$ and $(Ru^{5+})_2O_9$ dimers, which do not maintain $d^{2.5}$ filling. Interestingly, the Li analog also exhibits a drop in susceptibility around 150 K, although this is not associated with a structural transition [18]; it is presently unclear whether charge-order occurs in this case. The Os analogues, $Ba_3B'Os_2O_9$ (B′ = Na, Li), have also been reported [19]. Both compounds show no evidence of charge order, whereas kinks in the susceptibility around 10–13 K likely indicate magnetic ordering. Curie-Weiss fits yield larger effective moments of about 5 μ_B for the ruthenates [18] and lower effective moments of about 3.3 μ_B for the osmates [19]. However, all values should be taken with caution because, similar to the $d^{3.5}$ iridates, large antiferromagnetic Weiss constants suggest that the true paramagnetic regime has not been reached, and/or the effective moment is strongly temperature dependent.

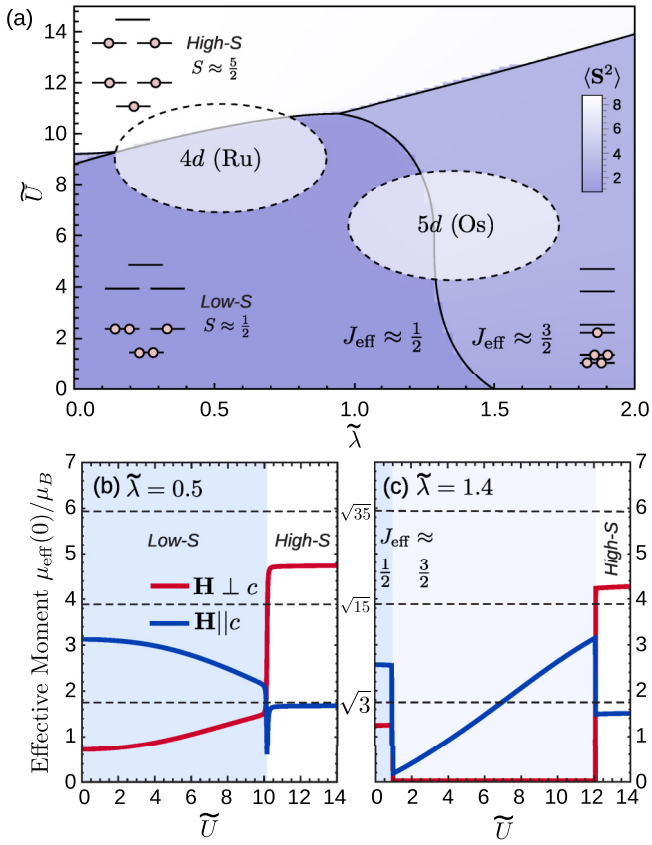

FIG. 7. (a) Phase diagram of theoretical ground state of a $d^{2.5}$ dimer as a function of $\tilde{U} = U/t_2$ and $\tilde{\lambda} = \lambda/t_2$ for $t_1 = \Delta = 0$. We fix $J_H/U = 0.18$. (b, c) Evolution of the zero-temperature effective moment as a function of $\tilde{U}$ for $\tilde{\lambda}$ values corresponding to 4d and 5d materials, respectively.

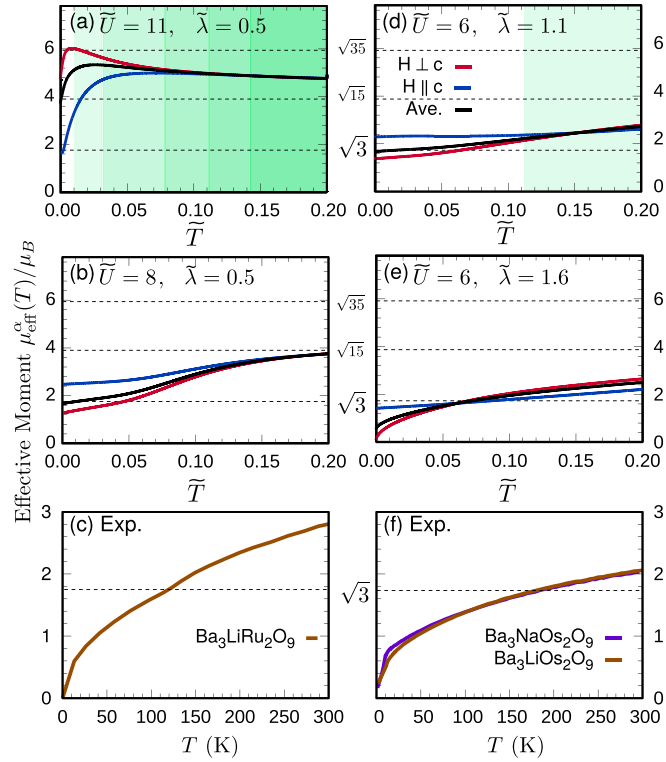

FIG. 8. Temperature dependence of the magnetic moments for $d^{2.5}$ dimers with various $\tilde{U}\,(U/t_2)$ and $\tilde{\lambda}(\lambda/t_2)$ values for $t_1 = \Delta = 0$. (a, b) Theoretical results for isolated 4d dimers in high-spin and low-spin ground states, respectively. The green area displays the region where excited states are filled. (c) Experimental effective moment for $Ba_3LiRu_2O_9$ based on data from Ref. [18]. (d, e) Theoretical results for isolated 5d dimers in $J_{\rm eff} \approx 1/2$ and $J_{\rm eff} \approx 3/2$ ground states, respectively. The energy of the first excited state is above 0.2 t_2. (f) Experimental effective moment for $Ba_3(Na/Li)Os_2O_9$ derived from Ref. [19].

B. Phase diagram

The theoretical phase diagram for $d^{2.5}$ filling and $\Delta = t_1 = 0$ is shown in Fig. 7(a). The green areas display the lowest five excited states region. In the nonrelativistic limit $\tilde{\lambda} \to 0$, these materials also exhibit high-spin and low-spin states depending on the strength of interactions. For the high-spin $S = 5/2$ state, there is one electron in each antibonding e_g ($e_{3/2}$, $e_{5/2}$) and bonding e_g ($e_{1/2}$, $e_{3/2}$) and bonding a_g ($e_{1/2}$) orbitals. At lowest order, the orbital momentum is quenched. In contrast, the low-spin state consists of all five electrons in the bonding orbitals, while the antibonding levels are empty. The degenerate bonding e_g levels contain three electrons, leading to an unquenched orbital degree of freedom. However, in this case, the unpaired electron nominally occupies a level with $j_{1/2}$ character, identifying this ground state as $J_{\rm eff} \approx 1/2$.

The evolution of $\mu_{\rm eff}(0)$ as a function of $\tilde{U}$ is shown in Fig. 7(b) for $\tilde{\lambda} = 0.5$, corresponding to a reasonable value for Ru-based dimers.The energy of the first excited state is above 0.2 t_2. For the high-spin state, the introduction of a small λ leads to a splitting of the six degenerate states into three pairs of Kramers doublets. The $m_s = \pm 1/2$ states form the ground state, which leads to $\mu^{ab}_{\rm eff} > \mu^{c}_{\rm eff} \approx \sqrt{3}$. In contrast, the low-spin state has a reversed anisotropy of the effective moment. This finding can be understood from the single-particle levels. For small λ, the single unpaired electron occupies an $e_{1/2}$ orbital with mostly $j_{1/2}$ character, leading to a $J_{\rm eff} \approx 1/2$ ground state. The average effective moment is then $\approx \sqrt{3}$, with an anisotropy $\mu^{ab}_{\rm eff} < \mu^{c}_{\rm eff}$ due to mixing with $J_{\rm eff} \approx 3/2$ states.

Considering the ordering of single-particle levels also provides a description of the third phase appearing at large $\tilde{\lambda}$ in the phase diagram. For small $\tilde{U}$ and large $\tilde{\lambda}$, a single unpaired electron occupies an $e_{3/2}$ antibonding level of pure $j_{3/2}$ character, suggesting a $J_{\rm eff} \approx 3/2$ ground state. The complete sequence of ground states can be seen in the evolution of $\mu_{\rm eff}(0)$ for $\tilde{U} = 1.4$, shown in Fig. 7(c). For intermediate values of $\tilde{U}$, the $J_{\rm eff} \approx 3/2$ ground state shows a suppressed effective moment, with $\mu^{ab}_{\rm eff} = 0$. This reflects the fact that this doublet is essentially composed of $m_J = \pm 3/2$ states. These Ising-like moments acquire a finite $\mu^{c}_{\rm eff}$ due to Hund's coupling, but the transverse moment is essentially zero. We expect that Os-based dimers may lie near the border of $J_{\rm eff} \approx 3/2$ region and $J_{\rm eff} \approx 1/2$ region.

C. Comparison to experiment

In Fig. 8, we show the computed temperature dependence of the effective moment for selected parameters corresponding to regions expected for real materials. In the strongly relativistic region relevant for Os-based dimers, the anisotropy of $\mu_{\rm eff}$ is generally weak. In Figs. 8(d) and 8(e), we show the temperature dependence of $\mu_{\rm eff}$ for $\tilde{\lambda} = 1.1$ and 1.6, corresponding to the $J_{\rm eff} \approx 1/2$ and $J_{\rm eff} \approx 3/2$ ground states, respectively. The green area in Fig. 8(d) shows the region where the first excited state is filled. The energy of the first excited state in Fig. 8(e) is above $0.2\ t_2$. For the later case, the suppressed $\mu^{ab}_{\rm eff}$ discussed above is observed only at relatively low temperatures, below room temperature ($\tilde{T} = T/t_2 \sim 0.1$). The theoretical results can be compared with the experimental $\sqrt{(3k_BT/N_A)\chi_{\rm avg}(T)}$ for $Ba_3BOs_2O_9$ (B = Na, Li) based on data from Ref. [19] shown in Fig. 8(f). In principle, the experimental powder data may be consistent with both possible ground states; single-crystal measurements may be more valuable in the future.

For Ru-based dimers, there is a stark contrast between the behavior of the high-spin $S \approx 5/2$ [Fig. 8(a)] and low-spin $J_{\rm eff} \approx 1/2$ [Fig. 8(b)] cases. The first case shows a nonmonotonic average effective moment, with significant anisotropy at low temperatures. At high temperatures, the average value is somewhat suppressed below the spin-only value of $\sqrt{35}\mu_B$ due to SOC. In contrast, in the low-spin case, $\mu^{\alpha}_{\rm eff}(T)$ evolves monotonically, is more weakly anisotropic, and has average value comparable to a pure $J_{\rm eff} = 1/2$ moment of $\sqrt{3}$. These results can be compared to the experimental $\mu_{\rm eff}(T)$ of $Ba_3LiRu_2O_9$, shown in Fig. 8(c), which is based on measurements of the powder susceptibility in Ref. [18]. For the entire temperature range, the average experimental effective moment remains on the order of $\sqrt{3}$, which suggests that either the material is in a low-spin state, or has a strongly suppressed moment due to strong interdimer couplings or incipient charge order.

VII. SUMMARY AND CONCLUSION

In this work, we considered the theoretical phase diagrams and magnetic response of face-sharing dimers of $4d$ and $5d$ elements with fractional fillings $d^{2.5}$ to $d^{4.5}$. On the basis of these studies we draw various conclusions.

(i) For these complex materials with competing Coulomb, hopping, and SOC terms, the magnetic response of individual dimers exhibits strong departures from conventional Curie behavior. As a result, Curie-Weiss analysis of the magnetic susceptibility may not be applicable or, if applied, will return strange results that do not reflect true nature of the local magnetic moment. Except for the most standard case of large $\tilde{U}$ and small $\tilde{\lambda}$, essentially all interaction regimes considered in our study lead to effective moments that are strongly temperature dependent up to at least $\tilde{T} = 0.1$, which corresponds to room temperature and represents the typical range of the Curie-Weiss fitting of the experimental data. In this situation, analyzing the temperature-dependent effective moment can be a better strategy that yields valuable information regarding the local electronic ground states of the dimers. The data above room temperature and experimental information on the anisotropy will strongly improve the accuracy of such an analysis.

(ii) The ground states of the dimers depend on the relative values of Coulomb interactions J_H, U, spin-orbit coupling strength λ, and intradimer hoppings t_1, and t_2. An important consideration is that increasing λ leads to several crossings of single-particle levels of different symmetry, which manifests in phase transitions between different ground-state configurations depending on the specific filling. From the experimental perspective, this level crossing leads to electronic excitations lying within the energy range of 50–100 meV and accessible for inelastic neutron scattering, which can provide additional valuable information on the electronic structure. It also justifies the application of empirical models that were used to describe magnetic susceptibility of mixed-valence dimers in terms of excitations between several electronic states [16,22]. A caveat here is that none of these states feature purely spin moments, so their energies and magnetic moments should be both treated as fitting parameters, with the risk of making the model overparameterized.

(iii) For all considered fillings, $4d$ Ru- and Rh-based dimers may, in principle, exhibit either low-spin or high-spin ground states. From a survey of available experimental susceptibility data, we find that the vast majority of such materials likely fall into a low-spin ground state. Provided C_3 symmetry of the dimers is maintained, all low-spin states have unquenched orbital moments, which strongly modify the magnetic response via coupling to the $S = 1/2$ degrees of freedom. Thus, consideration of SOC is essential for these materials. Intradimer charge order, previously suggested to exist in some of these materials, is unnecessary to explain the strong suppression of the effective magnetic moments.

(iv) For $5d$ materials, various ground states are possible, having either pure $J_{\rm eff} = 3/2$ character, or mixed $J_{\rm eff} = 1/2$ and $J_{\rm eff} = 3/2$ character. Identifying the nature of these local degrees of freedom is an essential prerequisite for establishing minimal magnetic models for these materials. For the case of the spin-liquid candidate material $Ba_3InIr_2O_9$ with $d^{4.5}$ filling of the Ir sites, the magnetic response is suggestive of a "low-spin" $J_{\rm eff} \approx 3/2$ ground state. Once the ground-state configuration can be further confirmed, for example via RIXS, analysis of the interdimer couplings would be of significant interest. The temperature dependence of the susceptibility can be modelled as arising from predominantly single-dimer effects, which would be consistent with relatively weak interdimer magnetic couplings.

We hope that this discussion provides a comprehensive overview of the properties of face-sharing $4d$ and $5d$ dimers with fractional fillings, which may serve as a starting point for future experimental and theoretical studies of these complex materials.

ACKNOWLEDGMENTS

We thank Daniel Khomskii, Igor Mazin, Sergey V. Streltsov, Markus Grüninger, and Adam A. Aczel for discussions and acknowledge the support by the Deutsche Forschungsgemeinschaft (DFG) through Grant No. VA117/15-1. Computer time was allotted at the Centre for for

TABLE I. Partial character table for D_{3h} double group [41].

	E	C_3	$3C_2'$	σ_h	S_6	$3\sigma_v$	$\overline{E}$	$\overline{C}_3$	$\overline{S}_6$
$E_{1/2}$	2	1	0	0	$\sqrt{3}$	0	−2	−1	$-\sqrt{3}$
$E_{3/2}$	2	−2	0	0	0	0	−2	2	0
$E_{5/2}$	2	1	0	0	$-\sqrt{3}$	0	−2	−1	$\sqrt{3}$

Scientific Computing (CSC) in Frankfurt. R.V. and S.M.W. acknowledge support from the National Science Foundation under Grant No. NSF PHY-1748958 and hospitality from KITP where part of this work was performed. Y.L. acknowledges support from the Fundamental Research Funds for the Central Universities (Grant No. xxj032019006), China Postdoctoral Science Foundation (Grant No. 2019M660249), and National Natural Science Foundation of China (Grant No. 12004296). The work in Augsburg was supported by DFG via Project No. 107745057 (TRR80) and by the Federal Ministry for Education and Research through the Sofja Kovalevskaya Award of Alexander von Humboldt Foundation (A.A.T.)

APPENDIX A: CHARACTER TABLE FOR D_{3h} DOUBLE GROUP

A character table for the states of $e_{1/2}$, $e_{3/2}$, and $e_{5/2}$ is given in Table I [41].

APPENDIX B: DETAILS OF CRYSTAL GROWTH AND CHARACTERIZATION FOR $Ba_3InIr_2O_9$

Small single crystals of $Ba_3InIr_2O_9$ were grown from the prereacted polycrystalline material in the $BaCl_2$ flux taken in the 1:10 ratio. The mixture was heated to 1200° C in 9 hours and kept at this temperature for 20 hours followed by a slow cooling to 950 °C in 90 hours and a standard furnace cooling to room temperature. The resulting crystals had platelet hexagonal form and linear dimensions of less than 0.3 mm. They showed the same lattice parameters and hexagonal symmetry as the powder samples reported previously [22]. Energy-dispersive x-ray spectroscopy (EDXS) analysis revealed the element ratio of In:Ir:Ba = 1:2.08(6):3.17(9) in good agreement with the $Ba_3InIr_2O_9$ composition. The *c*-direction of the crystals was determined by monitoring reflections on the x-ray powder diffractometer (Rigaku MiniFlex, CuK_α radiation).

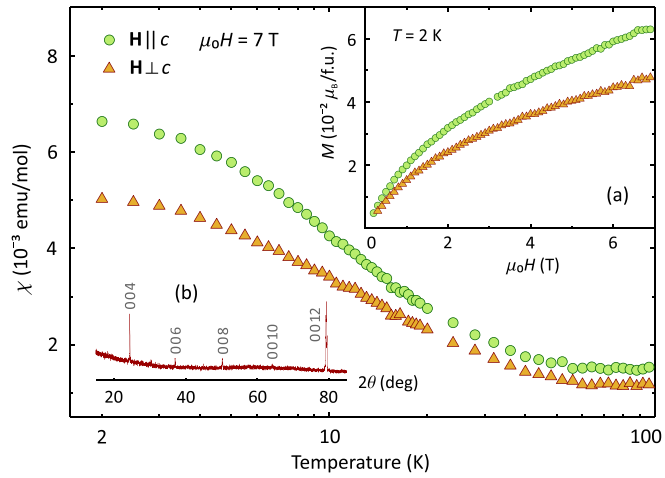

FIG. 9. Temperature-dependent magnetic susceptibility measured on the $Ba_3InIr_2O_9$ single crystal in the applied field of 7 T for different field directions. Inset (a): Field-dependent magnetization at 2 K. Inset (b): X-ray diffraction pattern from the [001] surface of the crystal.

Magnetic susceptibility (Fig. 9) was measured on a single crystal using the MPMS3 superconduting quantum interference device (SQUID) magnetometer from Quantum Design in the temperature range of 1.8–200 K in the applied field of 7 T. Above 200 K, the signal was below the sensitivity limit, owing to the very small sample size. As the sample mass could not be determined with sufficient accuracy, the data measured for $H \parallel c$ and $H \perp c$ were averaged and scaled against the powder data. The powder data were measured up to 650 K, as explained in Ref. [22].

[1] W. Witczak-Krempa, G. Chen, Y. Kim, and L. Balents, Correlated quantum phenomena in the strong spin-orbit regime, Annu. Rev. Condens. Matter Phys. **5**, 57 (2014).
[2] J. Rau, E.-H. Lee, and H.-Y. Kee, Spin-orbit physics giving rise to novel phases in correlated systems: Iridates and related materials, Annu. Rev. Condens. Matter Phys. **7**, 195 (2016).
[3] R. Schaffer, E. K.-H. Lee, B.-J. Yang, and Y. B. Kim, Recent progress on correlated electron systems with strong spin-orbit coupling, Rep. Prog. Phys. **79**, 094504 (2016).
[4] S. Winter, A. Tsirlin, M. Daghofer, J. van den Brink, Y. Singh, P. Gegenwart, and R. Valentí, Models and materials for generalized Kitaev magnetism, J. Phys.: Condens. Matter **29**, 493002 (2017).
[5] G. Cao and P. Schlottmann, The challenge of spin-orbit-tuned ground states in iridates: A key issues review, Rep. Prog. Phys. **81**, 042502 (2018).
[6] J. Darriet, M. Drillon, G. Villeneuve, and P. Hagenmuller, Interactions magnétiques dans des groupements binucléaires du Ruthénium +V, J. Solid State Chem. **19**, 213 (1976).
[7] Q. Chen, S. Fan, K. Taddei, M. Stone, A. Kolesnikov, J. Cheng, J. Musfeldt, H. Zhou, and A. Aczel, Large positive zero-field splitting in the cluster magnet $Ba_3CeRu_2O_9$, J. Amer. Chem. Soc. **141**, 9928 (2019).
[8] A. J. Kim, H. O. Jeschke, P. Werner, and R. Valentí, **J** Freezing and Hund's Rules in Spin-Orbit-Coupled Multiorbital Hubbard Models, Phys. Rev. Lett. **118**, 086401 (2017).
[9] A. Nag, S. Middey, S. Bhowal, S. K. Panda, R. Mathieu, J. C. Orain, F. Bert, P. Mendels, P. G. Freeman, M. Mansson, H. M. Ronnow, M. Telling, P. K. Biswas, D. Sheptyakov, S. D. Kaushik, V. Siruguri, C. Meneghini, D. D. Sarma, I. Dasgupta, and S. Ray, Origin of the Spin-Orbital Liquid State in a Nearly $J = 0$ Iridate $Ba_3ZnIr_2O_9$, Phys. Rev. Lett. **116**, 097205 (2016).

[10] A. Nag, S. Bhowal, M. M. Sala, A. Efimenko, I. Dasgupta, and S. Ray, Hopping-Induced Ground-State Magnetism in 6*H* Perovskite Iridates, Phys. Rev. Lett. **123**, 017201 (2019).

[11] R. C. Byrne and C. W. Moeller, Magnetic interactions of ruthenium, rhodium, and iridium in the hexagonal barium titanate structure, J. Solid State Chem. **2**, 228 (1970).

[12] Y. Doi and Y. Hinatsu, The structural and magnetic characterization of 6H-perovskite-type oxides $Ba_3LnIr_2O_9$ (Ln = Y, lanthanides), J. Phys.: Condens. Matter **16**, 2849 (2004).

[13] T. Sakamoto, Y. Doi, and Y. Hinatsu, Crystal structures and magnetic properties of 6H-perovskite-type oxides $Ba_3MIr_2O_9$ (M = Mg, Ca, Sc, Ti, Zn, Sr, Zr, Cd and In), J. Solid State Chem. **179**, 2595 (2006).

[14] Y. Doi, K. Matsuhira, and Y. Hinatsu, Crystal structures and magnetic properties of 6H-perovskites $Ba_3MRu_2O_9$ (M = Y, In, La, Sm, Eu, and Lu), J. Solid State Chem. **165**, 317 (2002).

[15] M. S. Senn, S. A. J. Kimber, A. M. Arevalo Lopez, A. H. Hill, and J. P. Attfield, Spin orders and lattice distortions of geometrically frustrated 6H-perovskites $Ba_3B'Ru_2O_9$ (B' = La^{3+}, Nd^{3+}, and Y^{3+}), Phys. Rev. B **87**, 134402 (2013).

[16] D. Ziat, A. A. Aczel, R. Sinclair, Q. Chen, H. D. Zhou, T. J. Williams, M. B. Stone, A. Verrier, and J. A. Quilliam, Frustrated spin-$\frac{1}{2}$ molecular magnetism in the mixed-valence antiferromagnets $Ba_3MRu_2O_9$ (M = In, Y, Lu), Phys. Rev. B **95**, 184424 (2017).

[17] S.-J. Kim, M. D. Smith, J. Darriet, and H.-C. zur Loye, Crystal growth of new perovskite and perovskite related iridates: $Ba_3LiIr_2O_9$, $Ba_3NaIr_2O_9$, and $Ba_{3.44}K_{1.56}Ir_2O_{10}$, J. Solid State Chem. **177**, 1493 (2004).

[18] K. E. Stitzer, M. D. Smith, W. R. Gemmill, and H.-C. zur Loye, Novel mixed-valent (V/VI) triple perovskite ruthenates: Observation of a complex low-temperature structural and magnetic transition, J. Amer. Chem. Soc. **124**, 13877 (2002).

[19] K. E. Stitzer, A. E. Abed, M. D. Smith, M. J. Davis, S.-J. Kim, J. Darriet, and H.-C. zur Loye, Crystal growth of novel osmium-containing triple perovskites, Inorg. Chem. **42**, 947 (2003).

[20] L. Shlyk, S. Kryukov, V. Durairaj, S. Parkin, G. Cao, and L. De Long, Magnetic, and electronic properties of a $Ba_3InRu_2O_9$ single crystal, J. Magn. Magn. Mater. **319**, 64 (2007).

[21] A. Nag and S. Ray, Misjudging frustrations in spin liquids from oversimplified use of curie-weiss law, J. Magn. Magn. Mater. **424**, 93 (2017).

[22] T. Dey, M. Majumder, J. C. Orain, A. Senyshyn, M. Prinz-Zwick, S. Bachus, Y. Tokiwa, F. Bert, P. Khuntia, N. Büttgen, A. A. Tsirlin, and P. Gegenwart, Persistent low-temperature spin dynamics in the mixed-valence iridate $Ba_3InIr_2O_9$, Phys. Rev. B **96**, 174411 (2017).

[23] S. V. Streltsov and D. I. Khomskii, Covalent bonds against magnetism in transition metal compounds, Proc. Natl. Acad. Sci. **113**, 10491 (2016).

[24] S. V. Streltsov and D. I. Khomskii, Orbital-dependent singlet dimers and orbital-selective peierls transitions in transition-metal compounds, Phys. Rev. B **89**, 161112(R) (2014).

[25] K. I. Kugel, D. I. Khomskii, A. O. Sboychakov, and S. V. Streltsov, Spin-orbital interaction for face-sharing octahedra: Realization of a highly symmetric su(4) model, Phys. Rev. B **91**, 155125 (2015).

[26] D. I. Khomskii, K. I. Kugel, A. O. Sboychakov, and S. V. Streltsov, Role of local geometry in the spin and orbital structure of transition metal compounds, J. Exp. Theor. Phys. **122**, 484 (2016).

[27] B. S. Tsukerblat, A. Tarantul, and A. Müller, Antisymmetric exchange and pseudo jahn-teller instability in spin-frustrated metal clusters, J. Mol. Struct. **838**, 124 (2007), proceedings of the Symposium on the Jahn-Teller Effect.

[28] K. Foyevtsova, H. O. Jeschke, I. I. Mazin, D. I. Khomskii, and R. Valentí, *Ab initio* analysis of the tight-binding parameters and magnetic interactions in Na_2IrO_3, Phys. Rev. B **88**, 035107 (2013).

[29] S. M. Winter, Y. Li, H. O. Jeschke, and R. Valentí, Challenges in design of kitaev materials: Magnetic interactions from competing energy scales, Phys. Rev. B **93**, 214431 (2016).

[30] A. Banerjee, C. A. Bridges, J.-Q. Yan, A. A. Aczel, L. Li, M. B. Stone, G. E. Granroth, M. D. Lumsden, Y. Yiu, J. Knolle, S. Bhattacharjee, D. L. Kovrizhin, R. Moessner, D. A. Tennant, D. G. Mandrus, and S. E. Nagler, Proximate Kitaev quantum spin liquid behavior in a honeycomb magnet, Nat. Mater. **15**, 733 (2016).

[31] B. H. Kim, G. Khaliullin, and B. I. Min, Electronic excitations in the edge-shared relativistic Mott insulator: Na_2IrO_3, Phys. Rev. B **89**, 081109(R) (2014).

[32] M. Kotani, On the magnetic moment of complex ions. (I), J. Phys. Soc. Jpn. **4**, 293 (1949).

[33] T. Dey, R. Kumar, A. V. Mahajan, S. D. Kaushik, and V. Siruguri, Unconventional magnetism in the spin-orbit-driven Mott insulators $Ba_3MIr_2O_9$ (M = Sc, Y), Phys. Rev. B **89**, 205101 (2014).

[34] S. K. Panda, S. Bhowal, Y. Li, S. Ganguly, R. Valentí, L. Nordström, and I. Dasgupta, Electronic structure and spin-orbit driven magnetism in $d^{4.5}$ insulator $Ba_3YIr_2O_9$, Phys. Rev. B **92**, 180403(R) (2015).

[35] R. Kumar, D. Sheptyakov, P. Khuntia, K. Rolfs, P. G. Freeman, H. M. Rønnow, T. Dey, M. Baenitz, and A. V. Mahajan, $Ba_3M_xTi_{3-x}O_9$ (M = Ir, Rh): A family of $5d/4d$-based diluted quantum spin liquids, Phys. Rev. B **94**, 174410(R) (2016).

[36] A. Revelli, M. M. Sala, G. Monaco, P. Becker, and L. Bohaty, Resonant inelastic x-ray incarnation of young's double-slit experiment, Sci. Adv. **5**, eaav4020 (2019).

[37] Y. Doi, Y. Hinatsu, Y. Shimojo, and Y. Ishii, Crystal structure and magnetic properties of 6H-perovskite $Ba_3NdRu_2O_9$, J. Solid State Chem. **161**, 113 (2001).

[38] Q. Chen, A. Verrier, D. Ziat, A. J. Clune, R. Rouane, X. Bazier-Matte, G. Wang, S. Calder, K. M. Taddei, C. R. dela Cruz, A. I. Kolesnikov, J. Ma, J.-G. Cheng, Z. Liu, J. A. Quilliam, J. L. Musfeldt, H. D. Zhou, and A. A. Aczel, Realization of the orbital-selective mott state at the molecular level in $Ba_3LaRu_2O_9$, Phys. Rev. Materials **4**, 064409 (2020).

[39] H.-C. zur Loye, S.-J. Kim, R. Macquart, M. D. Smith, Y. Lee, and T. Vogt, Low temperature structural phase transition of $Ba_3NaIr_2O_9$, Solid State Sci. **11**, 608 (2009).

[40] S. A. J. Kimber, M. S. Senn, S. Fratini, H. Wu, A. H. Hill, P. Manuel, J. P. Attfield, D. N. Argyriou, and P. F. Henry, Charge Order at the Frontier between the Molecular and Solid States in $Ba_3NaRu_2O_9$, Phys. Rev. Lett. **108**, 217205 (2012).

[41] G. F. Koster, Space Groups and Their Representations, Phys. Rev. B. Solid State **5**, 173 (1957).